Quasi-Static Behavior of Individual C-Block Piezoelectric Actuators

ANDREW J. MOSKALIK AND DIANN BREI*
Department of Mechanical Engineering and Applied Mechanics, The University of Michigan, 2250 G. G. Brown, Ann Arbor, MI 48109-2125

ABSTRACT: Most piezoelectric actuators used in smart structure applications are either stiff stacks which produce high forces and small deflections, or compliant benders which produce large deflections and small forces. This leaves a mid-range gap in actuator performance in which many applications operate. A new class of solid state actuators, known as C-blocks, has been developed as a mid-range actuator. A C-block is a semicircular composite bender actuated with piezoelectric layers. It can be combined in series and/or parallel to increase actuator deflection and/or force. A simple, linear analytical model for the quasi-static force-deflection behavior of a generic individual C-block is presented in this paper. This model can be used to determine the relationship between force and deflection, as well as the free deflection, blocking force, actuator stiffness, and maximum energy transferable to the actuated system. This model was experimentally verified with three case studies: PZT-8 and PZT-5H ceramic unimorphs; PVdF polymeric bimorphs; and four-layer PVdF polymeric multimorphs. The results from these case studies confirm that C-blocks are over six times stiffer, and generate over two-and-a-half times more force than a comparable straight bender.

INTRODUCTION

In the last decade, a number of new actuator applications have appeared in the field of smart structures, including active vibration damping of wings (Kudva et al., 1996) and helicopter rotor blades (Samak and Chopra, 1993), missile fin actuation (August and Joshi, 1996), active noise control (Fuller and Gibbs, 1994), vibration control in precision machining (Martinez, Hinnerichs, and Redmind, 1996), micropositioning (Yang, Jouaneh, and Schweizer, 1996), active automotive suspensions (Thirupathi and Naganathan, 1992) and active engine mounts (Sumali and Cudney, 1994). The success of these applications depends on efficient energy transfer from the driving actuator to the application system. Giurgiutiu, Chaudhry, and Rogers (1995) showed that the proportion of energy from the actuator available for external work, represented in Figure 1 by the shaded area, is maximized when the stiffnesses of the driving actuator and the external system are properly matched. Figure 1 shows a typical force-deflection model for a piezoelectric actuator. This graph contains important design and operation information for the actuation system. The actuator blocking force (with deflection held to zero) can be found along the vertical axis, or force axis, and the free deflection (with force held to zero) can be found along the horizontal axis, or deflection axis. In addition to the identification of force and deflection levels, the slope of the force-deflection model can be used to find the stiffness of the actuator. With proper stiffness matching of the actuator to the external system, the energy transfer is maximized. Thus, one of the most important tools for selection of an appropriate actuator in many applications is the force-deflection model.

A common actuator type used in smart structure applications are piezoelectric actuators because they are small, have low power requirements, respond quickly, and generate relatively high forces (Baz and Poh, 1988; Damjanovic and Newnham, 1992). For these actuators, the stiffness, and thus energy characteristics, are fixed by the design and material parameters chosen for a specific actuator configuration. Standard piezoelectric actuator architectures fall into one of two categories: compliant benders, which produce large deflections but small forces; and stiff stacks, which produce high forces but small deflections. A mid-range stiffness gap exists between these two architectures where many actuator applications operate. A common scheme used to create a mid-range stiffness actuator for many applications involves mechanical leveraging of stacks (Bamford et al., 1995; Samak and Chopra, 1996) to improve deflection performance at the expense of force generation capability, thereby making the overall stack actuator package more compliant. However, this approach frequently suffers from transmission losses (Paine and Chaudhry, 1996) and may create difficulties in packaging the additional external leveraging mechanisms. A variety of other approaches have been recently proposed to fill the mid-range stiffness gap, such as tapered bender beams (Hall and Prechtl, 1996), RAINBOW actuators (Haertling, 1994), moonie actuators (Onitsuka et al., 1995), and cymbal actuators (Dogan, Uchino, and Newnham, 1997). However, there still remains a need in this field for small size actuators with mid-range stiffness.

*Author to whom correspondence should be addressed.

1045-389X/97/07 0571-17 $10.00/0

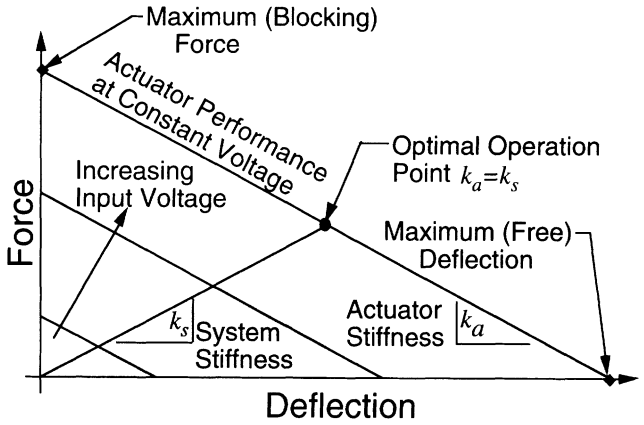

Figure 1. *Force-deflection model for a generic piezoelectric actuator. This shows the interrelationship among voltage input, force output, and deflection output. The optimal operation point is located where the stiffnesses of the actuator and system are matched. The maximum output energy is represented by the shaded area.*

C-blocks have been proposed as mid-range stiffness actuators. C-blocks are curved laminate piezoelectric bender actuators. Prior research (Brei, 1994, 1995a, 1995b) on these actuator architectures has been primarily conducted using symmetric bimorph C-blocks fabricated from a polymeric material, Polyvinylidene Fluoride (PVdF). This preliminary research has shown that a C-block architecture can develop greater blocking force with a slight reduction in free deflection when compared to the commonly used straight bender architecture. PVdF, however, is an inherently compliant material with limited force generation capabilities. The limited force output of PVdF bimorph C-blocks can be improved by increasing the number of piezoelectric layers in the C-block, resulting in a stiffer structure (Moskalik and Brei, 1995), or by fabricating C-blocks out of piezoceramic material. Piezoceramics are stiffer than polymeric materials and possess a higher piezoelectric constant (d_{31}), making piezoceramics better suited to many smart structure applications. A unimorph C-block configuration has been developed (Brei, Ervin, and Moskalik, 1996) where a single layer of piezoceramic is bonded to an inert substrate, thus providing bending actuation while keeping the ceramic in compression. Past characterization of these unimorph piezoceramic C-blocks has included investigation of deflection performance, but until now has not included the complete force-deflection model. The force-deflection model is a major design tool that not only provides force and deflection information as a function of voltage, but also defines the C-block stiffness for correct stiffness matching, allowing engineers to design C-block actuators for operation at the optimum energy transfer point in a smart structures system.

Thus, the next step in the investigation of the C-block architecture is the characterization of the force-deflection performance of a general C-block actuator, and is the topic of this paper. This paper presents both an analytical and experimental characterization of the force deflection behavior of a generic piezoelectric C-block, which includes bimorphs, unimorphs, and more complex multilayered architectures. A simple analytical model is derived by solving the equations of equilibrium generated using Hamilton's principle. This model is instrumental in comparing C-blocks to the commonly used straight bender. The analytical model was experimentally validated with three force-deflection case studies: PZT unimorph C-blocks, PVdF bimorph C-blocks, and four-layered PVdF multimorph C-blocks.

A GENERIC C-BLOCK ACTUATOR ARCHITECTURE

A generic C-block architecture can consist of an arbitrary number of layers laminated together and configured into a semicircular shape, as shown in Figure 2. The layers within the C-block can consist of active piezoelectric elements (sensors and actuators), and inert layers (electrodes, bonding layers and substrates). The active piezoelectric elements are poled in the radial direction and arranged such that all elements on one side of the neutral axis strain in the opposite direction to those on the other side. When a voltage is applied to the actuator, the piezoelectric material strains in the circumferential direction to create a bending moment which causes the actuator to flex.

The semicircular shape allows C-blocks to be combined in a variety of actuator architectures to improve their force and deflection performance (Brei, 1994, 1995a, 1995b), as shown in Figure 3. To increase the free deflection without changing the maximum blocking force, C-blocks can be connected in series. Likewise, to increase the blocking force without affecting the free deflection, C-blocks can be combined in parallel. To increase both the output force and deflection, C-blocks are combined both in series and in parallel to form a distributed array architecture. These architectures can be used to alter the stiffness of the actuator as shown in Figure 3, with the stiffness being increased in a parallel configuration or decreased in a series configuration. Thus, with the wide number of discrete actuator combinations possible, a distributed C-block array architecture has the potential to be tailored to match the stiffness of the external system while simultaneously producing the target force and deflection required, and fitting within the application space available.

This design flexibility is one of the foremost attractions of

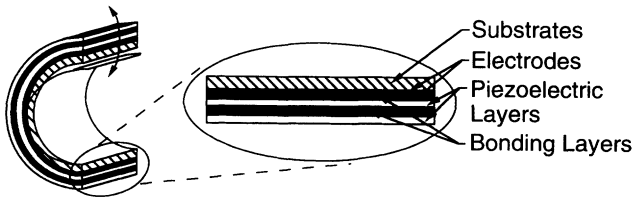

Figure 2. *A generic individual C-block actuator architecture. A C-block architecture is comprised of a variety of active and inactive layers, where the active layers strain, making the C-block flex. This figure gives an example of one lay-up from the vast number of available options.*

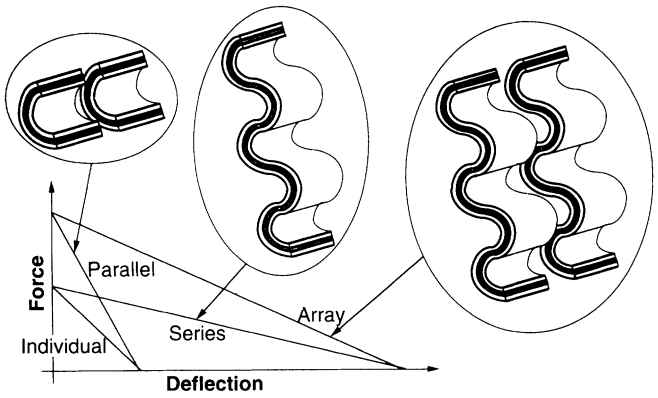

Figure 3. *C-block actuator architectures. C-block actuators can be combined into architectures, where parallel architectures are more stiff, delivering greater force; series architectures are less stiff, delivering greater displacement; and distributed array architectures are variably stiff, potentially delivering greater force and deflection.*

the C-block. To model the performance of a distributed C-block array architecture, it is necessary to begin by modeling the behavior of an individual C-block, which is the basic unit of the distributed array structure. Also, for some applications, an individual C-block may be the best choice for an actuator if an array structure is not necessary. Thus, derivation and experimental verification of a force-deflection model for a generic individual C-block is essential both for laying groundwork necessary in predicting the behavior of larger distributed arrays of C-blocks, and for describing the performance of individual C-block actuators.

ANALYTICAL MODEL

The analytical model that defines the relationship between the force and deflection output of an individual C-block unit was derived using an energy approach. During the derivation, one objective was to produce a model of simple form that can be easily used by engineers designing actuators. Thus, the C-block was assumed to have a thin cross-section, and was modeled as a cantilevered, curved laminate beam

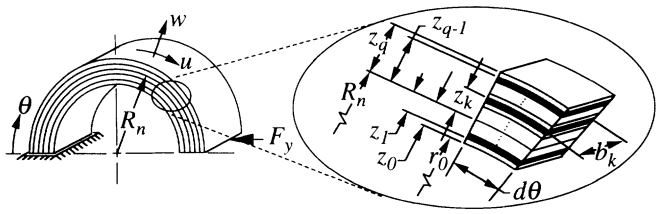

Figure 4. *Analytical model nomenclature. Nomenclature used for a general C-block of* q *layers with an applied force* F_y. *The constants* u *and* w *are the circumferential and radial displacements, respectively,* θ *is the angular coordinate,* O *is the origin,* r *is the radius from the origin to the outside of the layer,* R_n *is the neutral axis radius,* z *is the distance from the neutral axis to the outside of the layer, and* b *is a layer width. The layers are numbered sequentially in the subscript, with the subscript 0 referring to the inside surface,* q *referring to the outside surface and* k *referring to an arbitrary interior surface.*

with q perfectly bonded layers, a constant radius, and total angular span of π radians. It was assumed that strain energy was stored only in bending and extensional strains, and that transverse shear effects were negligible. The nomenclature used in the derivation is shown in Figure 4, where u and w are the circumferential and radial deflections, respectively, θ is an angular coordinate, R_n is the distance from the origin, O, to the neutral axis, b is a layer width, r is the distance from the origin to the outside of a layer, z is the distance from the neutral axis to the outside of a layer ($z = r - R_n$), and F_y is the external force required at the C-block tip to balance the internally generated piezoelectric load.

To model a generic individual C-block, the equations of equilibrium were obtained using Hamilton's principle in a method similar to that employed by Qatu (1993) for non-piezoelectric laminated curved beams; however, piezoelectric terms were included in the constitutive equation as described by Larson and Vinson (1993). Although both of these prior researchers derived equations of equilibrium for curved beams similar in form to the C-block, they neither investigated the specific boundary conditions of the cantilever case used for the C-block nor developed a final model relating force and deflection. To use Hamilton's principle in deriving the governing equations for the C-block, expressions for the internal stress and strain within the C-block were found and these expressions were used to define the strain energy. The strain energy, along with the external work, were combined using Hamilton's principle to obtain equations of equilibrium and the associated boundary conditions. These equations and boundary conditions were solved to develop the quasi-static force-deflection model for the C-block. The development of the force-deflection model is described in more detail below.

Strain Energy

Hamilton's principle requires the formulation of an expression for the potential energy within the C-block. The potential energy is comprised of work done by external forces and the strain energy stored within the C-block. Focusing first on the strain energy, the approach for formulating the strain energy is to integrate the stress multiplied by the strain throughout the volume of the C-block. The resulting strain energy formulation is simplified by determining expressions for the internal normal force, internal moment, and the location of the neutral axis. The details of this approach follow.

CONSTITUTIVE LAW

The first step in formulating the strain energy is to derive an expression for the stress within the C-block. For one-dimensional strain, the magnitude of the stress in the circumferential direction at any point in the C-block is given by the piezoelectric constitutive law, where the stress is the Young's modulus multiplied by the strain,

$$\sigma = Y(\varepsilon_m + d_{31}E_3) \tag{1}$$

In Equation (1), Y is the Young's modulus of the material and $d_{31}E_3$ is the internally induced piezoelectric strain. The electric field, E_3, is defined as positive if it is applied in the same direction as the polarity of the material and negative if applied in the opposite direction. The piezoelectric constant, d_{31}, relates the electric field in the radial direction to circumferential strains. In poled piezoelectric ceramics, d_{31} is negative, and in nonactive materials it is assumed to be zero.

For a thin C-block, the strain induced by mechanical loads, ε_m, is modeled by assuming a linear strain profile through the cross-section. Thus, the expression for strain at a distance z from the neutral axis is,

$$\varepsilon_m = \varepsilon^0 + z\kappa \tag{2}$$

where ε^0 is the strain at the neutral axis, κ is the change in curvature, and z is the distance to the neutral axis. The total internal stress is found by inserting the value of the mechanical strain [Equation (2)] into the piezoelectric constitutive equation [Equation (1)] to yield

$$\sigma = Y(\varepsilon^0 + z\kappa + d_{31}E_3) \tag{3}$$

which is the value of the stress at any point in the C-block a distance z from the neutral axis.

STRAIN ENERGY EXPRESSION

The internal stress [Equation (3)] is used to derive an expression for the strain energy stored in the C-block. The total strain energy is one-half the volume integral of the stress multiplied by the strain at each point in the C-block,

$$U = \frac{1}{2}\int_V Y\left[\varepsilon^{0^2} + (z\kappa)^2 + (d_{31}E_3)^2 + 2\varepsilon^0 z\kappa + 2\varepsilon^0 d_{31}E_3 + 2z\kappa d_{31}E_3\right]dV \tag{4}$$

Hamilton's principle uses the variance of the energy in the system; thus, the objective is to determine the variance of the strain energy rather than the energy itself. The variance of the strain energy shown in Equation (4) is

$$\delta U = \int_V Y[(\varepsilon^0 + z\kappa + d_{31}E_3)\delta\varepsilon^0 + (z\varepsilon^0 + z^2\kappa + zd_{31}E_3)\delta\kappa]dV = \int_V (\sigma\delta\varepsilon^0 + \sigma z\delta\kappa)dV \tag{5}$$

INTERNAL NORMAL FORCE AND MOMENT

The variance of the strain energy [Equation (5)] is simplified by defining an expression for the normal force and moment that includes integrals of the stress. The normal force at any cross-section in the C-block is defined as the stress [Equation (3)] integrated over the cross-sectional area, A,

$$N = \int_A \sigma dA = \int_A Y(\varepsilon^0 + z\kappa + d_{31}E_3)dA \tag{6}$$

Because the C-block is a composite structure, the integration must be performed piecewise over the cross-sectional area. Integrating the normal force [Equation (6)] across the q layers of the composite cross-sectional area yields,

$$N = \sum_{i=1}^{q} Y_i b_i (z_i - z_{i-1})\varepsilon^0 + \sum_{i=1}^{q} \frac{1}{2} Y_i b_i (z_i^2 - z_{i-1}^2)\kappa + \sum_{i=1}^{q} Y_i b_i (z_i - z_{i-1})(d_{31}E_3)_i \tag{7}$$

where the subscript i refers to the ith layer: b_i is the width of the ith layer, Y_i is the Young's modulus of the ith layer, and z_i is the distance from the neutral axis to the outside of the ith layer.

Calculated in a similar way to the normal force, the moment about the neutral axis is defined as the stress [Equation (3)] multiplied by a moment arm to the neutral axis, z, and integrated over the cross-sectional area,

$$M = \int_A \sigma z dA = \int_A Y(\varepsilon^0 + z\kappa + d_{31}E_3)zdA \tag{8}$$

Integrating the moment Equation (8) piecewise across the composite cross-sectional area yields,

$$M = \sum_{i=1}^{q} \frac{1}{2} Y_i b_i (z_i^2 - z_{i-1}^2)\varepsilon^0 + \sum_{i=1}^{q} \frac{1}{3} Y_i b_i (z_i^3 - z_{i-1}^3)\kappa + \sum_{i=1}^{q} \frac{1}{2} Y_i b_i (z_i^2 - z_{i-1}^2)(d_{31}E_3)_i \tag{9}$$

The normal force and moment [Equations (7) and (9)] are restated more succinctly as,

$$\begin{Bmatrix} N \\ M \end{Bmatrix} = \begin{bmatrix} A & B \\ B & D \end{bmatrix} \begin{Bmatrix} \varepsilon^0 \\ \kappa \end{Bmatrix} + \begin{Bmatrix} N^P \\ M^P \end{Bmatrix} \tag{10}$$

where the constants A, B, and D are the stiffnesses calculated during the integration of the normal force and moment [Equations (6) and (8)] and are defined as,

$$A = \sum_{i=1}^{q} Y_i b_i (z_i - z_{i-1}); \quad B = \sum_{i=1}^{q} \frac{1}{2} Y_i b_i (z_i^2 - z_{i-1}^2)$$
$$\text{and} \quad D = \sum_{i=1}^{q} \frac{1}{3} Y_i b_i (z_i^3 - z_{i-1}^3) \tag{11}$$

Likewise, the piezoelectric forcing terms M^P and N^P are defined as,

$$N^P = \sum_{i=1}^{q} Y_i b_i (z_i - z_{i-1})(d_{31} E_3)_i$$
$$\text{and} \quad M^P = \sum_{i=1}^{q} \frac{1}{2} Y_i b_i (z_i^2 - z_{i-1}^2)(d_{31} E_3)_i \tag{12}$$

where $d_{31} = 0$ in the non-piezoelectric layers.

LOCATION OF NEUTRAL AXIS

The stiffnesses [Equation (11)] and forcing terms [Equation (12)] are defined in terms of the locations within the C-block, z, as measured from the neutral axis. Thus, the location of the neutral axis must be defined. The neutral axis is the surface in the C-block that experiences no stress in pure bending, because the internal forces above and below the neutral axis location cancel. Thus, the location of the neutral axis is found by setting the internal force to zero, assuming no piezoelectric extensional strains, and finding the location within the cross-section where the mechanical strain is zero. This results in the definition of the neutral axis as,

$$R_n = \frac{\sum_{i=1}^{q} \frac{1}{2} Y_i b_i (r_i^2 - r_{i-1}^2)}{\sum_{i=1}^{q} Y_i b_i (r_i - r_{i-1})} \tag{13}$$

where r_i is the radius from the origin to the ith layer. Choosing the neutral axis as a reference point also simplifies the expressions for normal force and moment [Equation (10)]. When z is measured from the neutral axis, the stiffnesses are symmetric. Substituting Equation (13) into the coupling stiffness B, defined in Equation (11) shows that this stiffness reduces to zero, thus simplifying the normal force and moment [Equation (10)] to

$$\begin{Bmatrix} N \\ M \end{Bmatrix} = \begin{bmatrix} A & 0 \\ 0 & D \end{bmatrix} \begin{Bmatrix} \varepsilon^0 \\ \kappa \end{Bmatrix} + \begin{Bmatrix} N^P \\ M^P \end{Bmatrix} \tag{14}$$

SIMPLIFIED STRAIN ENERGY

Using the definitions of normal force [Equation (6)] and moment [Equation (8)], the variance of the strain energy [Equation (5)] is simplified from a volume integral to an integral in the angular coordinate θ,

$$\delta U = \int_0^{\pi} (N \delta \varepsilon^0 + M \delta \kappa) R_n d\theta \tag{15}$$

To produce the equations of equilibrium, the strain energy variance equation is restated in terms of the circumferential, u, and radial, w, displacements rather than strain and curvature change. The relations among the neutral axis displacements, strain, and curvature change are

$$\varepsilon^0 = \frac{1}{R_n} (u_{,\theta} + w); \quad \text{and} \quad \kappa = \frac{1}{R_n^2} (-w_{,\theta\theta} + u_{,\theta}) \tag{16}$$

where the subscript ",θ" refers to differentiation with respect to the circumferential coordinate, θ. Substituting the displacement relations [Equation (16)] into the variance of the potential energy [Equation (15)] results in,

$$\delta U = \int_0^{\pi} \left[N \delta u_{,\theta} + N \delta w - \frac{M}{R_n} \delta w_{,\theta\theta} + \frac{M}{R_n} \delta u_{,\theta} \right] d\theta \tag{17}$$

In Hamilton's principle, the integrand must contain no differentials of the virtual displacements δu or δw. Integration by parts allows Equation (17) to be restated as,

$$\delta U = \left\{ \int_0^{\pi} \left[-N_{,\theta} \delta u + N \delta w - \frac{M_{,\theta\theta}}{R_n} \delta w - \frac{M_{,\theta}}{R_n} \right] d\theta \right\}$$
$$+ \left[N \delta u - \frac{M}{R_n} \delta w_{,\theta} + \frac{M_{,\theta}}{R_n} \delta w + \frac{M}{R_n} \delta u \right]_0^{\pi} \tag{18}$$

Potential Energy

The strain energy expressed in Equation (18) is one portion of the potential energy. The total potential energy of the C-block is the difference between the strain energy contained within the C-block and the work from external forces. The external work term arises from the product of the external force, F_y, shown in Figure 4, and the distance that force travels. The variation of this work is

$$\delta W = -F_y \delta w|_{\pi R} \tag{19}$$

The variation of the potential energy, δV, is the difference between the variation of the strain energy [Equation (18)] and the variation of the work [Equation (19)]

$$\delta V = \left\{ \int_0^{\pi} \left[-N_{,\theta}\delta u + N\delta w - \frac{M_{,\theta\theta}}{R_n}\delta w - \frac{M_{,\theta}}{R_n}\delta u \right] d\theta \right\}$$

$$+ \left[N\delta u - \frac{M}{R_n}\delta w_{,\theta} + \frac{M_{,\theta}}{R_n}\delta w + \frac{M}{R_n}\delta u \right]_0^{\pi} + F_y \delta w|_{\pi} \tag{20}$$

Equations of Equilibrium and Boundary Conditions

Hamilton's principle states that the time integral of the difference in the variation of the potential energy and kinetic energy is zero,

$$\int_{t_1}^{t_2} (\delta T - \delta V) dt = 0 \tag{21}$$

For this quasi-static force-deflection model, the kinetic energy, and its variation, are zero. Substituting the variation of the potential energy [Equation (20)] into Hamilton's principle [Equation (21)], results in

$$\int_{t_1}^{t_2} \left\{ \int_0^{\pi} \left[N_{,\theta}\delta u - N\delta w + \frac{M_{,\theta\theta}}{R_n}\delta w + \frac{M_{,\theta}}{R_n}\delta u \right] d\theta \right.$$

$$+ \left[-N\delta u + \frac{M}{R_n}\delta w_{,\theta} - \frac{M_{,\theta}}{R_n}\delta w - \frac{M}{R_n}\delta u \right]_0^{\pi}$$

$$\left. - F_y \delta w|_{\pi} \right\} dt = 0 \tag{22}$$

EQUATIONS OF EQUILIBRIUM

Hamilton's principle [Equation (22)] contains the equations of equilibrium and the associated boundary conditions for the C-block. Since δu and δw are arbitrary, the terms multiplying them must be zero. The terms multiplying these variances within the spatial integral in Hamilton's principle [Equation (22)] are the equations of equilibrium,

$$\frac{N_{,\theta}}{R_n} + \frac{M_{,\theta}}{R_n^2} = 0 \quad \text{and} \quad -\frac{N}{R_n} + \frac{M_{,\theta\theta}}{R_n^2} = 0 \tag{23}$$

These equations are restated in terms of the displacement using the definitions of the moment and normal force [Equation (14)] along with the relations among the displacements, extensional strain, and curvature change [Equation (16)],

$$\left(\frac{1}{\chi} + 1\right) u_{,\theta\theta\theta} + \frac{1}{\chi} w_{,\theta} - w_{,\theta\theta\theta} = 0$$

$$u_{,\theta\theta\theta} - \frac{1}{\chi} u_{,\theta} - \frac{1}{\chi} w - w_{,\theta\theta\theta} = \frac{N^P R_n^3}{D} \tag{24}$$

where the nondimensional stiffness parameter, χ, is the ratio of the bending stiffness to the extensional stiffness,

$$\chi = \frac{D}{AR_n^2} \tag{25}$$

where A and D are defined in Equation (11). Since the piezoelectric forcing terms are constant with respect to θ, the only piezoelectric forcing term appearing in the equations of equilibrium is the N^P from the undifferentiated normal force in the second equation.

BOUNDARY CONDITIONS

Both the piezoelectric moment and normal force, however, do appear in the boundary conditions. There are six boundary conditions associated with this system of equations, which are found from Hamilton's principle [Equation (22)]. Since δu and δw are arbitrary, each term outside of the spatial integral in Equation (22) must vanish independently. At $\theta = 0$, the C-block is clamped, so the appropriate boundary conditions are

$$w|_0 = 0; \quad w_{,\theta}|_0 = 0; \quad \text{and} \quad u|_0 = 0 \tag{26}$$

and, at $\theta = \pi$, the end is free with an applied force F_y, so the appropriate boundary conditions are

$$M|_{\pi} = 0; \quad \left.\frac{M_{,\theta}}{R_n}\right|_{\pi} + F_y = 0; \quad \text{and} \quad \left.\left(N + \frac{M}{R_n}\right)\right|_{\pi} = 0 \tag{27}$$

Since $M|_{\pi} = 0$, the last boundary condition reduces to $N|_{\pi} = 0$. When the definitions of the moment and normal force [Equation (14)] along with the relations among the displacements, extensional strain, and curvature change [Equation (16)] are applied to the free end boundary conditions, the resulting boundary conditions are,

$$\left[\frac{D}{R_n^2}(-w_{,\theta\theta} + u_{,\theta}) + M^P\right] = 0$$

$$\left[\frac{D}{R_n^3}(-w_{,\theta\theta\theta} + u_{,\theta\theta})\right]_{\pi} + F_y = 0 \tag{28}$$

$$\text{and} \quad \left[\frac{D}{\chi R_n^3}(u_{,\theta} + w) + N^P\right]_{\pi} = 0$$

where the stiffness ratio χ has been used to simplify the last boundary condition.

Quasi-Static Force-Deflection Model

The equations of equilibrium [Equation (24)] and boundary conditions [Equations (26) and (28)] are solved to develop the quasi-static force-deflection model for the C-block. The solution is the sum of a particular solution and independent homogeneous solutions.

HOMOGENEOUS SOLUTIONS

The coupled equations of equilibrium [Equation (24)] possess a corresponding characteristic determinate, the roots of which are used to determine the homogeneous solutions. To find the homogeneous solutions, the equations of equilibrium are restated as an eigenvalue problem by setting the forcing term to zero,

$$\begin{bmatrix} \left(\frac{1}{\chi}+1\right)\frac{\partial^2}{\partial\theta^2} & \frac{1}{\chi}\frac{\partial}{\partial\theta}-\frac{\partial^3}{\partial\theta^3} \\ -\frac{1}{\chi}\frac{\partial}{\partial\theta}+\frac{\partial^3}{\partial\theta^3} & -\frac{1}{\chi}-\frac{\partial^4}{\partial\theta^4} \end{bmatrix}\begin{pmatrix} u \\ w \end{pmatrix} = \begin{pmatrix} 0 \\ 0 \end{pmatrix} \tag{29}$$

where the terms of the matrix in Equation (29) are differential operators acting upon u and w. The homogeneous solutions to these equations of equilibrium are assumed to be of exponential form,

$$\begin{pmatrix} u_n \\ w_n \end{pmatrix} = \begin{pmatrix} U_n \\ W_n \end{pmatrix} e^{\eta_n \theta} \tag{30}$$

When this solution [Equation (30)] is applied to the eigenvalue problem [Equation (29)], the exponential factors cancel. The resulting determinant is equated to zero,

$$\frac{1}{\chi}\eta^6 + \frac{2}{\chi}\eta^4 + \frac{1}{\chi}\eta^2 = 0 \tag{31}$$

to find the homogeneous solutions. The roots of this determinant are three pairs of repeated roots: 0, 0, i, i, $-i$, and $-i$. There are six possible solutions which form the complete homogeneous solution when summed,

$$\begin{pmatrix} u_h \\ w_h \end{pmatrix} = \begin{pmatrix} U_1 \\ W_1 \end{pmatrix} + \theta\begin{pmatrix} U_2 \\ W_2 \end{pmatrix} + \begin{pmatrix} U_3 \\ W_3 \end{pmatrix} e^{i\theta} + \theta\begin{pmatrix} U_4 \\ W_4 \end{pmatrix} e^{i\theta} + \begin{pmatrix} U_5 \\ W_5 \end{pmatrix} e^{-i\theta} + \theta\begin{pmatrix} U_6 \\ W_6 \end{pmatrix} e^{-i\theta} \tag{32}$$

An equivalent form of the solution using transcendental functions is,

$$\begin{pmatrix} u_h \\ w_h \end{pmatrix} = \begin{pmatrix} \beta_1 \\ \alpha_1 \end{pmatrix} \sin\theta + \begin{pmatrix} \beta_2 \\ \alpha_2 \end{pmatrix} \cos\theta + \begin{pmatrix} \beta_3 \\ \alpha_3 \end{pmatrix} \theta \sin\theta + \begin{pmatrix} \beta_4 \\ \alpha_4 \end{pmatrix} \theta \cos\theta + \begin{pmatrix} \beta_5 \\ \alpha_5 \end{pmatrix} + \begin{pmatrix} \beta_6 \\ \alpha_6 \end{pmatrix} \theta \tag{33}$$

PARTICULAR SOLUTION

In addition to the homogeneous solutions of Equation (33), a particular solution is required to account for the constant forcing term in the second equation of equilibrium [Equation (24)]. Since the forcing term is constant with respect to θ, it is convenient to account for the forcing term with a particular solution that is a constant,

$$\begin{pmatrix} u_p \\ w_p \end{pmatrix} = \begin{pmatrix} 0 \\ -\frac{N^P R_n^3 \chi}{D} \end{pmatrix} \tag{34}$$

where the particular solution of u is zero. This leads to a complete solution for u and w as the sum of the particular solution [Equation (34)] and the six homogeneous solutions [Equation (33)],

$$\begin{pmatrix} u \\ w \end{pmatrix} = \begin{pmatrix} \beta_1 \\ \alpha_1 \end{pmatrix} \sin\theta + \begin{pmatrix} \beta_2 \\ \alpha_2 \end{pmatrix} \cos\theta + \begin{pmatrix} \beta_3 \\ \alpha_3 \end{pmatrix} \theta \sin\theta + \begin{pmatrix} \beta_4 \\ \alpha_4 \end{pmatrix} \theta \cos\theta + \begin{pmatrix} \beta_5 \\ \alpha_5 \end{pmatrix} + \begin{pmatrix} \beta_6 \\ \alpha_6 \end{pmatrix} \theta + \begin{pmatrix} 0 \\ -\frac{N^P R_n^3 \chi}{D} \end{pmatrix} \tag{35}$$

The solutions for the radial and circumferential displacements contain a total of twelve unknown constants.

SUBSTITUTION INTO EQUATIONS OF EQUILIBRIUM

To solve for six of these unknowns, the complete displacement solution [Equation (35)] is substituted into one of the equations of equilibrium. Since the eigenvalues are repeated roots, it is convenient to insert the entire solution into the second equation of equilibrium, resulting in six independent equations relating the constants. Arbitrarily choosing to eliminate as many of the circumferential solution coefficients (β) as possible, the displacement equations [Equation (35)] become,

$$u = \left(-\alpha_2 + \frac{\chi-1}{\chi+1}\alpha_3\right)\sin\theta + \left(\alpha_1 + \frac{\chi-1}{\chi+1}\alpha_4\right)\cos\theta - \alpha_4\theta\sin\theta + \alpha_3\theta\cos\theta + \beta_5 - \alpha_5\theta \tag{36}$$

and

$$w = \alpha_1 \sin\theta + \alpha_2 \cos\theta + \alpha_3\theta \sin\theta + \alpha_4\theta \cos\theta + \alpha_5 - \frac{N^P R_n^3 \chi}{D} \tag{37}$$

APPLICATION OF BOUNDARY CONDITIONS

The final six constants are determined from the six boundary conditions [Equation (26) and (28)]. When the displacement equations [Equations (36) and (37)] are inserted into the boundary conditions, the resulting six independent equations are solved simultaneously to yield expressions for the remaining constants. Using these expressions, the final form of the circumferential displacement [Equation (36)] is

$$u = \left(\frac{M^P R_n^2}{D} - \frac{N^P R_n^3 \chi}{D}\right)\sin\theta - \frac{M^P R_n^2}{D}\theta - \frac{F_y R_n^3(\chi+1)}{2D}\theta \sin\theta + \frac{F_y R_n^3}{D}(1-\cos\theta) \tag{38}$$

and the final form of the radial displacement [Equation (37)] is

$$w = \frac{F_y R_n^3(\chi+1)}{2D}(\theta\cos\theta - \sin\theta) + \left(\frac{M^P R_n^2}{D} - \frac{N^P R_n^3 \chi}{D}\right)(1-\cos\theta) \tag{39}$$

C-BLOCK QUASI-STATIC FORCE-DISPLACEMENT MODEL

Since the C-block is assumed to be thin, the displacement equations may be simplified further. When the definition of χ from Equation (25) is expanded, using the stiffnesses A and D from Equation (11), and bringing the constant radius into the numerator, the definition of χ becomes

$$\chi = \frac{\sum_{i=1}^{q} \frac{1}{3} Y_i b_i \left(z_i \frac{z_i^2}{R_n^2} - z_{i-1}\frac{z_{i-1}^2}{R_n^2}\right)}{\sum_{i=1}^{q} Y_i b_i (z_i - z_{i-1})} \tag{40}$$

Comparing each term from the sum in the numerator to its counterpart in the denominator, the terms in the numerator are smaller by a factor of $(z_i/R_n)^2$. Therefore, when the thickness of the C-block is small in comparison to the radius, the denominator in Equation (40) is large, and $\chi \ll 1$. Thus, the term $(\chi + 1)$ in the displacement relations [Equations (38) and (39)] tends to one. Additionally, as Larson and Vinson (1993) observe, for thin curved beams constructed to be benders, χ is small enough that the normal force term can also be neglected in comparison to the moment term. Thus, the displacement equations [Equation (38) and (39)] are simplified to

$$u = \frac{M^P R_n^2}{D}(\sin\theta - \theta) - \frac{F_y R_n^3}{D}\left(\cos\theta - 1 + \frac{1}{2}\theta\sin\theta\right) \tag{41}$$

and

$$w = \frac{F_y R_n^3}{2D}(\theta\cos\theta - \sin\theta) + \frac{M^P R_n^2}{D}(1-\cos\theta) \tag{42}$$

Since the tip of the C-block is used most for actuation, it is useful to further simplify the displacement expressions to find the displacement expressly at the tip. The circumferential deflection at the tip, $u|_\pi$, is found by substituting π for θ in the general circumferential displacement equation [Equation (41)], resulting in,

$$u|_\pi = -\frac{\pi M^P R_n^2}{D} + \frac{2F_y R_n^3}{D} \tag{43}$$

Likewise, the radial deflection at the tip, $w|_\pi$, is found by substituting π for θ in the general radial displacement equation [Equation (42)], resulting in,

$$w|_\pi = \frac{2M^P R_n^2}{D} - \frac{F_y \pi R_n^3}{2D} \tag{44}$$

Because the incorporation of C-block actuators into a series configuration is expected to increase the displacement in the radial direction, it is the $w|_\pi$, component of the displacement that is of most interest. This equation [Equation (44)] is easily inverted to find the force available as a function of the deflection and the piezoelectric moment,

$$F_y = \frac{4M^P}{\pi R_n} - \frac{2Dw|_\pi}{\pi R_n^2} \tag{45}$$

PARAMETER ANALYSIS OF FORCE-DEFLECTION MODEL

This model is a simple representation of the behavior of the C-block throughout the force-deflection domain. The complete force-deflection model is obtained as a function of voltage by substituting the definitions of D and M^P [Equations (12) and (13)] into the general force-deflection model for a C-block [Equation (45)] to expand the expression for the force as a function of material and geometric parameters,

$$F_y = 2\sum_{j=1}^{q} \frac{b_j Y_j (d_{31} V)_j (z_j^2 - z_{j-1}^2)}{\pi R_n (z_j - z_{j-1})} - \frac{2\sum_{j=1}^{q} b_j Y_j (z_j^3 - z_{j-1}^3)}{3\pi R_n^3} w|_\pi \tag{46}$$

The simplification $E_3 = V/(z_j - z_{j-1})$ has been used, assuming the piezoelectric layers are thin compared to the radius. This general force-deflection model is applicable to any form of thin C-block actuator. The meaning of this equation is deduced by examining the dependence of the output force, F_y, on the parameters contained in the model [Equation (46)]. The force output comes from two sources: the first term is the piezoelectric forcing term and the second term is the stiffness relation. Since, for a particular actuator, all terms are constant except F_y, $w|_\pi$, and V, the general model relating force and deflection is seen to be a straight line, with an offset proportional to voltage and constant slope.

The slope of this line is the overall stiffness, from Equation (46), is the term relating the force and deflection,

$$k_c = \frac{2D}{\pi R_n^3} = \frac{2\sum_{j=1}^{q} b_j Y_j (z_j^3 - z_{j-1}^3)}{3\pi R_n^3} \qquad (47)$$

This stiffness is a function of the bending stiffness of the cross-section, D, and the neutral axis radius of the C-block. As the thickness of the C-block increases, the bending stiffness, and thus the overall stiffness, increases. As the radius increases, the overall stiffness decreases. Additionally, this collection of terms multiplying the deflection is always positive. Thus, from the general force-deflection model [Equation (46)], an increase in output deflection, $w|_\pi$, or stiffness, k_c, will result in a smaller output force, F_y.

The collection of terms comprising the piezoelectric forcing terms in Equation (46) is somewhat more complex. This term depends on the input voltage, the radius, and the size and stiffness of the piezoelectric layer. As expected, increasing the input voltage, piezoelectric constant, or the size or stiffness of the piezoelectric layers requires either the output force or the output deflection, or both to increase. C-blocks with a larger radius will have a smaller maximum (blocked) force output, but a larger displacement.

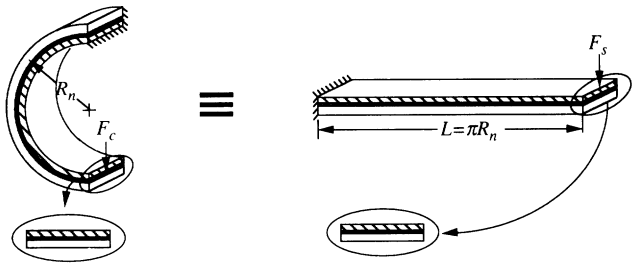

Figure 5. *Generic C-block and equivalent straight bender. A C-block is shown here with an equivalent straight bender, defined as having an identical cross-section, the same material volume, and a length of πR_n, and activated by an internally generated piezoelectric moment.*

Analytical Comparison of an Individual C-Block to an Equivalent Straight Bender

The force-deflection model [Equation (45)] enables the C-block to be compared to an equivalent straight bender architecture, which is frequently used in the smart structures field. An equivalent straight bender (Figure 5) is defined as having the same cross-section as the C-block and a length of πR_n, giving the actuator the same material volume. Four performance relations predicting the quasi-static performance of the individual C-block are developed using the force-deflection model [Equation (45)]: free deflection, blocking force, stiffness, and maximum application work. These expressions are given in Table 1. The free deflection expression is developed by setting the output force in the force-deflection model [Equation (45)] to zero. Likewise, the blocking force expression is developed by setting the deflection in the force-deflection model [Equation (45)] to zero. The stiffness [Equation (47)] relates the output deflection to

Table 1. Parameter comparison between C-block and straight bender actuators. C-blocks produce greater maximum (blocking) force, but less maximum (free) deflection than an equivalent straight bender. Additionally, the C-block is substantially stiffer, and produces more work than the straight bender.

	C-Block	Equivalent Straight Bender	Comparison Factor
Free deflection ($F = 0$)	$\Delta_c = \frac{2M^P R_n^2}{D}$	$\Delta_b = \frac{M^P \pi^2 R_n^2}{2D}$	$\Delta_c/\Delta_b = 0.405$
Blocking force ($\Delta = 0$)	$F_c = \frac{4M^P}{\pi R_n}$	$F_b = \frac{3M^P}{2\pi R_n}$	$F_c/F_b = 2.67$
Stiffness ($k = F/\Delta$)	$k_c = \frac{2D}{\pi R_n^3}$	$k_b = \frac{3D}{\pi^3 R_n^3}$	$k_c/k_b = 6.58$
Maximum work ($W = F\Delta/8$)	$W_c = \frac{(M^P)^2 R_n}{\pi D}$	$W_b = \frac{3(M^P)^2 \pi R_n}{32D}$	$W_c/W_b = 1.08$

the output force [Equation (45)]. Maximum application work is available from the actuator when the stiffness of the actuator and the application system are properly matched. The value of the maximum work is 0.125 times the product of the blocking force and the free deflection (Giurgiutiu, Chaudhry, and Rogers, 1995).

For the straight bender, expressions for these four quantities are easily obtained following a derivation procedure similar to that outlined for the individual C-block, and are well documented in the literature. The expressions for the performance parameters for the equivalent straight bender are given in Table 1. When the performance expressions for the C-block and the straight bender are compared, the C-block is 6.58 times as stiff, and produces 2.67 times the force, as the equivalent straight bender. The increase in force comes at the expense of deflection, as the C-block produces only 0.405 times the deflection as its straight counterpart. However, the total work that is available from the C-block is 8% more than the straight bender can produce; so overall the C-block compares favorably with the straight bender, and the greater stiffness and force output of the C-block positions it well as a mid-range actuation technology.

EXPERIMENTAL VALIDATION

To validate the analytical model for the radial force-deflection [Equation (44)] over a broad design range, three case studies were chosen: unimorph C-blocks fabricated from PZT-5H (soft) and PZT-8 (hard) piezoceramic, bimorph C-blocks fabricated from PVdF polymer, and four-layer multimorph C-blocks fabricated from PVdF polymer.

For the first case study, unimorph prototypes were fabricated from PZT-5H and PZT-8 piezoceramics. The PZT-5H chosen for this study was a standard grade of commercially available PZT purchased from Staveley Sensors and had a relatively high piezoelectric constant, d_{31}, when compared to other piezoelectric ceramics. The PZT-5H used had a Young's modulus of 63 GPa (Staveley) and a piezoelectric constant of -460 pm/V. The piezoelectric constant was determined for this material by measuring the ceramic with a Pennebaker Model 8000 d_{33} Tester. Because of the high piezoelectric constant, a large free displacement and a large blocking force at the tip of the prototype is produced. To present a contrast of properties, prototypes were also fabricated from PZT-8 piezoceramic. When compared to PZT-5H piezoceramic, the PZT-8 piezoceramic had a smaller d_{31} of -45.8 pm/V, a greater Young's modulus of 85 GPa (Staveley), higher breakdown voltage, reduced aging, and lower hysteresis. The piezoelectric constant for this material was also determined by using a d_{33} Tester. These differences offer a good contrast of properties between the prototypes tested.

Both types of PZT were fabricated into a unimorph design, shown in Figure 6(a), by bonding the ceramic to a steel substrate, with all of the ceramic material on one side of the neutral axis. The unimorph design was chosen because ceramics are weak in tension compared to their strength in compression. With the unimorph design, the ceramic experiences only compressive stresses during actuation, while the steel substrate absorbs the tensile stresses, thus eliminating the possibility of the ceramic failing in tension.

For the second case study, PVdF prototypes were constructed in a bimorph configuration as shown in Figure 6(b). The prototypes constructed for this case study were not only of a different, symmetric configuration, but there was a substantial contrast between the material properties of the PVdF and those of the piezoceramics. The Young's modulus of the epoxy bonding layer is 1.9 GPa, while the Young's modulus of the PVdF is 5.4 GPa, and the piezoelectric constant is 23 pm/V (Brei, 1995a). Since the bimorph prototypes were constructed so that the piezoelectric layers strain in opposite directions, the internal piezoelectric normal force present in the unimorph case study is eliminated, leaving only a net moment.

The third case study also used prototypes constructed from PVdF polymeric film. To present a greater contrast of geometric variables, the prototypes used in the third case study were constructed as four-layer multimorphs. For the prototypes used in this case study, the poling direction of the individual layers must be altered as shown in Figure 6(c) so that all layers on one side of the neutral axis strain opposite to those layers on the other side of the neutral axis. The proto-

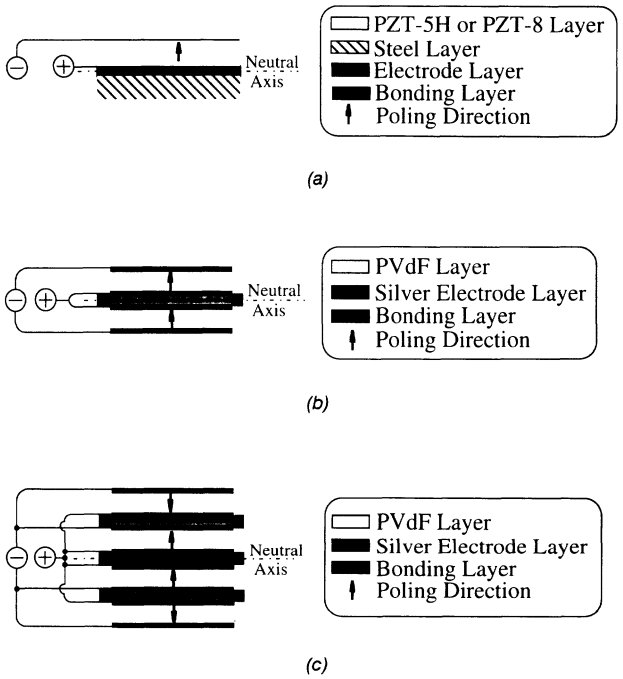

Figure 6. *Cross-sectional views of prototypes fabricated for each case study. (a) Case study 1: piezoceramic unimorph cross-section with steel substrate. (b) Case study 2: polymeric bimorph cross-section. PVdF layers are poled in the same direction and actuated with opposite electric field to create a net moment. (c) Case study 3: polymeric multimorph cross-section. The direction of the electric field is alternated between layers to keep adjacent electrodes at the same potential, thus requiring the poling pattern illustrated.*

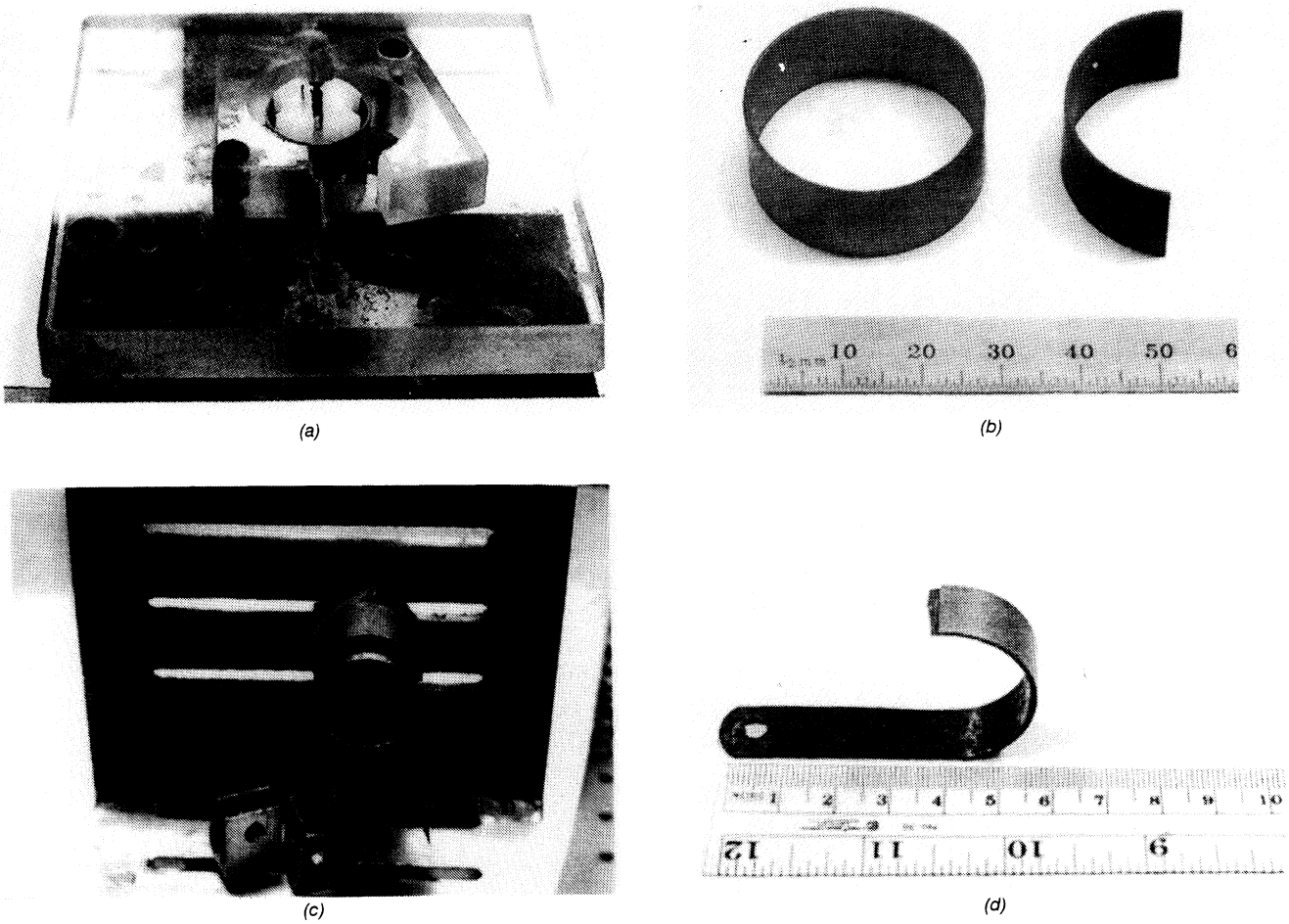

Figure 7. *Fabrication procedure for ceramic unimorph prototypes used in case study 1. (a) The piezoceramic tubes were placed in a fixture prior to sectioning with a diamond saw. (b) The diamond saw sliced the tubes into semicircles. (c) The sectioned ceramics were bonded to a U-shaped steel substrate with a layer of epoxy. (d) After the epoxy cured, the final ceramic prototypes were removed from the fixture and the steel substrate was trimmed.*

type fabrication, experimental procedures, and results for the polymeric and ceramic case studies are discussed separately below.

Case Study 1: Ceramic Unimorphs

The first case study used unimorph prototypes that were fabricated from two types of PZT piezoceramic material: PZT-5H and PZT-8. Prototypes made from both materials were fabricated and experimentally tested using identical methods.

PROTOTYPE FABRICATION

Each ceramic prototype was fabricated from a circular piezoceramic tube, either of PZT-5H or of PZT-8. Each tube measured 12.7 mm wide, 0.76 mm thick, and 15.88 mm in outside radius. The inner and outer radii of the tubes were pre-plated with a silver electrode a few microns thick. To fabricate the unimorph actuator, each tube was placed in a fixture, shown in Figure 7(a), and cut into two semicircular sections using a diamond saw. A sectioned tube is shown in Figure 7(b). A 0.406 mm thick steel strip was formed into a U-shape to conform to the inner diameter of the piezoceramic tube. The steel and the piezoceramic elements were fixtured together around a mandrel, shown in Figure 7(c), and bonded with an epoxy layer 85 microns thick. After the epoxy had cured, the final prototype, shown in Figure 7(d), was removed from the mandrel. Because the thickness of the electrode layers was significantly less than the thickness of the other layers in the C-block, the contribution of the electrode layer to the overall stiffness of the C-block was negligible, and thus was neglected in the model [Figure 6(a)]. Using the material and geometric parameters given, the nondimensional stiffness ratio, χ, was calculated to be 6.19 E-4 for the PZT-5H prototype and 6.35 E-4 for the PZT-8 prototype, confirming the assumption that this parameter is small.

EXPERIMENTAL PROCEDURE AND RESULTS

The laboratory setup used for testing of the ceramic prototypes is shown in Figure 8. Each prototype was rigidly clamped in place so that the radial movement of the C-block was in the horizontal direction. Lead wires were attached to

the prototype and connected directly to a high voltage DC power supply which was monitored with a digital multimeter. A force transducer was mounted to a precision stage that allowed the transducer to move in the radial direction of the C-block. The initial position of the tip of the prototype was recorded using the stage before any voltage was applied to the prototype. To test the PZT-5H prototype, voltages of 50 volts, 100 volts, and 150 volts were applied to the prototype, corresponding to electric fields of 65.8 V/mm, 131.6 V/mm, and 197.4 V/mm. To test the PZT-8 prototype, voltages in increments of 50 volts from 200 to 400 volts were used, corresponding to electric fields from 263.1 V/mm to 526.3 V/mm in increments of 65.8 V/mm. The higher maximum voltage was possible because of the greater breakdown voltage of the PZT-8 material. At each voltage level, the position of the tip of the prototype corresponding to zero force (the free deflection) was measured with the precision stage. The position of the stage was then incremented, with the force and position being recorded at each increment, until the tip deflection was returned to zero.

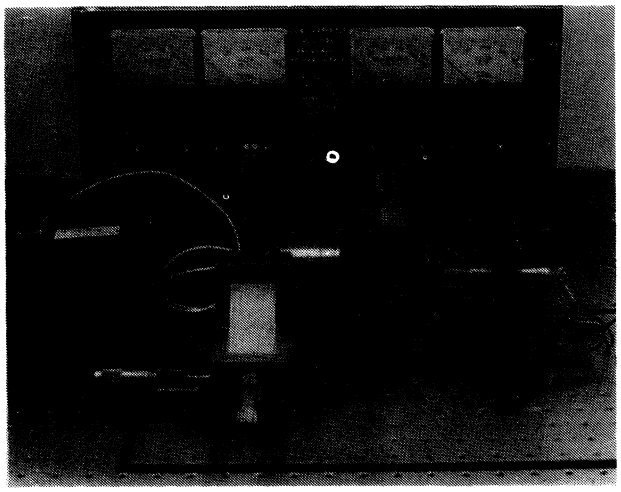

(a)

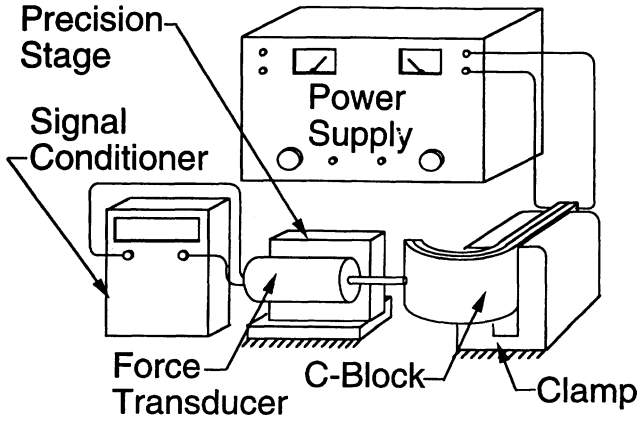

(b)

Figure 8. *Case study 1: experimental apparatus. This apparatus was used to test the force-deflection characteristics of the ceramic unimorph prototypes used in case study 1 and the polymeric multimorph prototypes used in case study 3. (a) The C-block prototype, force transducer, and stage are in the center of the picture; the DC power supply is in the background. (b) A schematic view of the equipment.*

The experimental results for both types of ceramic prototypes are shown in Figure 9, along with the performance predicted by the analytical model. Figure 9(a) shows the force-deflection experimental results for the PZT-5H ceramic prototype. The force-deflection plot in Figure 9(a) can be used to find the free deflection as a function of voltage by reading the horizontal axis intersections, and the blocking force can be found as a function of voltage by reading the vertical axis intersections. The maximum free deflection (at 150 V) is 48 microns, while the maximum blocked force is 1.93 Newtons. The graph shows the linear relationship between actuator output force and deflection as input voltage is held constant. The force-deflection lines generated at various voltages are parallel and evenly spaced, with the slope of the line indicating the stiffness of the actuator. As expected, the stiffness remains constant not only along each force-deflection line, but also across the various input voltages.

The results from the PZT-8 prototype, shown in Figure 9(b), are similar in form to the results from the PZT-5H piezoceramic. However, because of the substantially lower piezoelectric constant the maximum free deflection and blocking force are less than that of the PZT-5H piezoceramic, despite the higher voltages applied to the PZT-8 piezoceramic. The maximum free deflection (at 400 V) is 12.9 microns, while the maximum blocked force is 0.67 Newtons. The greater slope of the experimental lines in Figure 9(b) indicates that the stiffness of the PZT-8 prototype is greater than the stiffness of the PZT-5H, as would be expected from the larger Young's modulus of the piezoceramic.

Case Study 2: Polymeric Bimorphs

To present a strong contrast to the ceramic unimorph case study, the second case study used prototypes fabricated from PVdF polymeric material. Additionally, the prototypes constructed for the second case study were configured as a bimorph rather than a unimorph to broaden the design space explored.

PROTOTYPE FABRICATION

Unlike the ceramic prototypes, the polymeric prototypes were fabricated using a molding process. Two layers of 52 micron thick, 22 mm wide PVdF film were bonded together with a 17 micron thick layer of epoxy and formed around a dowel as shown in Figure 10(a). The film was pre-electroded with 6.5 micron thick, 17.5 mm wide silver electrode. The poling direction of the two layers was such that when voltage was applied, the strain in the layer above the neutral axis was opposite from the strain in the layer below [Figure 6(b)]. After the epoxy cured, the PVdF was removed from the dowel

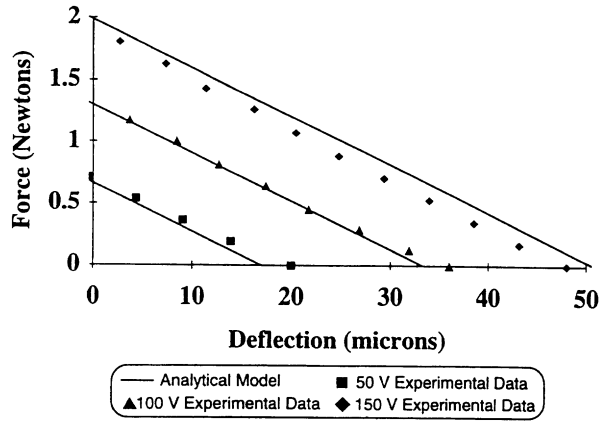

(a)

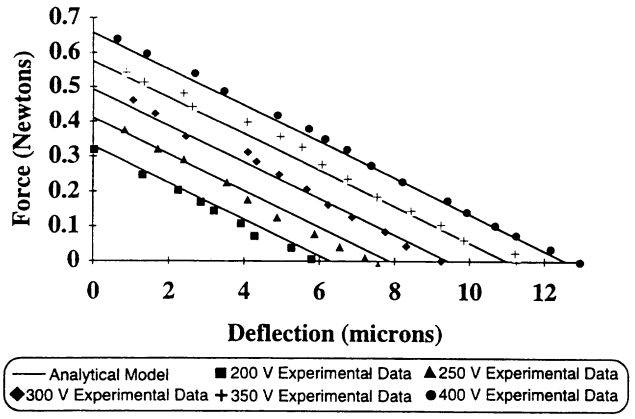

(b)

Figure 9. *Case study 1: experimental results. Experimental force-deflection results for the ceramic unimorph prototypes used in case study 1. (a) PZT-5H; outside radius = 15.88 mm; width = 12.7 mm; total thickness = 1.215 mm. (b) PZT-8; outside radius = 15.88 mm; width = 12.7 mm; total thickness = 1.25 mm.*

and the base was secured between glass slides to form a fixed end. A completed polymeric prototype is shown in Figure 10(b). The final outside radius of the C-block was 15.88 mm. Unlike in the ceramic prototypes, the thickness of the electrodes was not negligible when compared to the thickness of the other layers, and thus was included in the calculations for the stiffness. The nondimensional stiffness ratio, χ, for this polymeric prototype was 7.21 E-6, substantially smaller than in the ceramic prototypes.

EXPERIMENTAL PROCEDURE AND RESULTS

The stiffness of the polymeric prototype was much smaller than the stiffnesses of the ceramic prototypes; thus, the experimental procedure was altered. The test setup used for the polymeric bimorph prototypes is shown in Figure 11. For these C-blocks, the prototype was clamped in position so that the radial movement of the tip was in the vertical direction Lead wires were attached to the prototype and connected directly to a high voltage DC power supply which was monitored with a digital multimeter. The initial position of the tip of the prototype was recorded before any voltage was applied to the prototype by using a pointer attached to a calibrated scale. Voltages of 200 and 325 volts, corresponding to electric fields of 3.85 kV/mm and 6.25 kV/mm, were then applied to the prototype. At each voltage level, the position of the tip of the prototype corresponding to zero force (the free deflection) was found using the pointer. Weights were added to the tip in increments of 20 mg, and the position of the tip was recorded at each increment until the tip deflection was returned to zero.

The results from the bimorph PVdF prototype, shown in Figure 12, are similar in form to the results from the piezoceramic C-blocks; however, the maximum values vary greatly. The maximum free deflection (at 325 V) increased to 900 microns, while the maximum blocked force decreased to about 3.4 milliNewtons. The slope of the force-deflection lines in Figure 12 indicates that the stiffness of the polymeric bimorph is considerably less than the ceramic prototypes. This is because the Young's moduli of the constituent layers are lower as well as the layers themselves being much thinner.

Case Study 3: Polymeric Multimorphs

To further examine the validity of the model for multiple layers, a third case study focused on a simple multimorph with four layers. For ease in manufacturing and cost issues, PVdF was chosen as the piezoelectric material. Even though the lay-up for the multimorph differed from the bimorph case, a similar fabrication process was employed.

PROTOTYPE FABRICATION

First, the polymeric multimorph prototypes were fabricated using the same material and molding process as the bimorph. Four layers of pre-electroded 52 micron thick, 22 mm wide PVdF film were bonded together with 25 micron thick layers of epoxy and formed around a dowel. The poling direction of each layer was such that when voltage was applied, the strain in the layers above the neutral axis was opposite from the strain in the layers below [Figure 6(c)]. After the epoxy cured, the PVdF was removed from the dowel and the base was secured between glass slides to form a fixed end. The final outside radius of the C-block was 8.5 mm. Like the previous polymeric bimorph case study, the thickness of the electrodes was not negligible when compared to the thickness of the other layers, and thus was included in the calculations for the stiffness. The nondimensional stiffness ratio, χ, for this multimorph polymeric prototype was 1.42 E-4, a value between that for the ceramic unimorphs and the polymeric bimorphs. The stiffness ratio is higher for this case study than for the bimorph case study because the prototype was substantially thicker and had a smaller radius, both of which produce a stiffer C-block.

EXPERIMENTAL PROCEDURE AND RESULTS

Since the stiffness of this polymeric prototype was much greater than the stiffnesses of the bimorph polymeric proto-

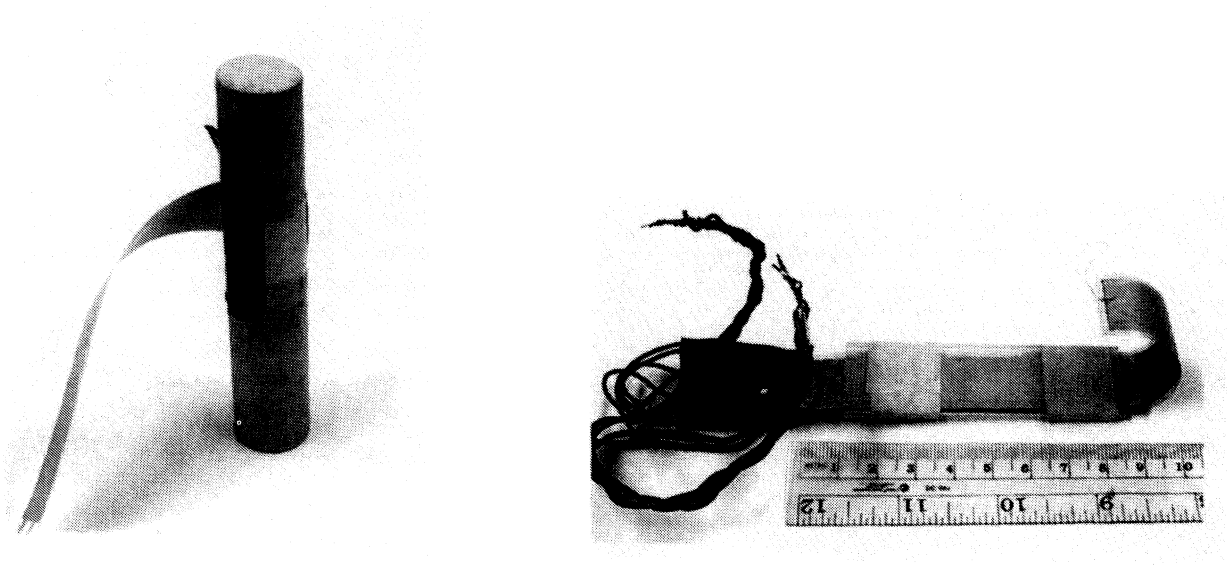

(a) (b)

Figure 10. *Fabrication procedure for polymeric bimorph and multimorph prototypes used in case studies 2 and 3. (a) The polymeric material was bonded together with epoxy and wrapped around a dowel. (b) After the epoxy had cured, the final polymeric prototypes were removed from the dowel, sandwiched between glass slides, and electrode wires were connected.*

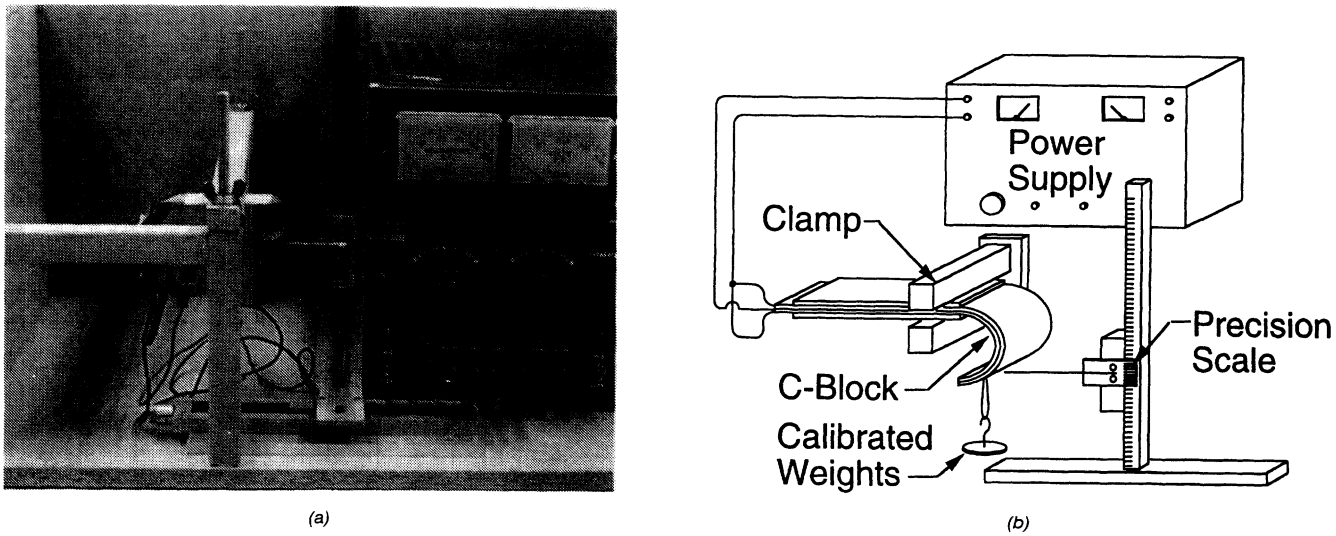

(a) (b)

Figure 11. *Case study 2: experimental apparatus. Experimental apparatus used to test the force-deflection characteristics of bimorph polymeric prototypes used in case study 2. (a) The C-block prototype, calibrated scale, and pointer are in the center of the picture; the DC power supply is in the background. (b) A schematic view of the equipment.*

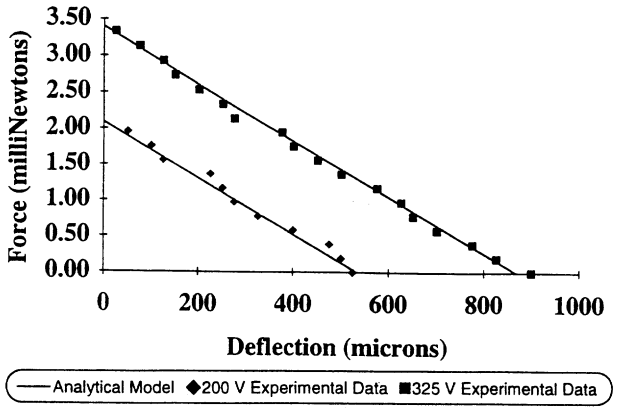

Figure 12. *Case study 2: experimental results. Experimental force-deflection results for the polymeric PVdF bimorph C-blocks used in case study 2. Outside radius = 15.88 mm; width = 17 mm; thickness = 0.335 mm.*

types used in case study 2, the experimental procedure used in this case study was similar to that for the PZT unimorph case study. The laboratory setup used for testing the prototypes of this case study is the same as the setup used in the first case study, and is shown in Figure 8. To measure the force-deflection response of the prototype, voltages in increments of 50 volts from 200 to 400 volts were used. At each voltage level, the position of the tip of the prototype corresponding to zero force (the free deflection) was found using the precision stage. The position of the stage was then incremented, with the force and position being recorded at each increment until the tip deflection was returned to zero.

The results from the PVdF prototype, shown in Figure 13, are similar in form to the results from the previous two C-block case studies. The maximum free deflection (at 400 V) is 140 microns, much less than for the polymeric bimorph, but greater than either of the ceramic case studies. The maximum blocked force of the multimorph is about 33 milliNewtons, an order of magnitude greater than the output from the

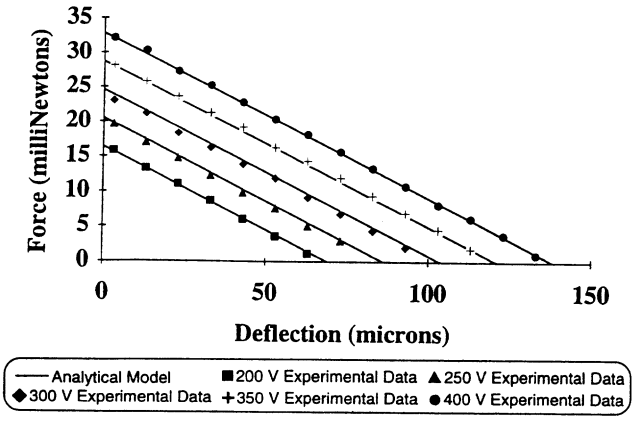

Figure 13. *Case study 3: experimental results. Experimental force-deflection results for the polymeric PVdF multimorph C-blocks used in case study 3. Outside radius = 8.5 mm; width = 22 mm; thickness = 0.147 mm.*

bimorph case study, but much smaller than the output from the ceramic case studies. This demonstrates the wide range of output possible from an individual C-block. The slope of the force-deflection lines in Figure 13 indicates that, as expected, the stiffness of the polymeric multimorph is considerably more than the bimorph case study, but less than the ceramic case study. The smaller radius and greater thickness of the multimorph make this prototype much stiffer than the bimorph; however, due to the lower Young's modulus of the polymeric and the thinner constituent layers, the overall stiffness of the multimorph prototypes is lower than the stiffness of the ceramic unimorphs.

DISCUSSION

The experimental results for the three case studies depicted in Figures 9, 12, and 13 show good correlation between the simple analytical force-deflection model presented in Equation (45) and the observed behavior of a C-block. The mean differences between the experimentally observed behavior of the prototypes (Figures 9, 12, and 13) and the analytical model are given in Table 2, both in units of Newtons and as a percentage of the maximum force output predicted by the analytical model. Overall, the observed behavior of the prototypes agrees well with the behavior predicted by the model, with the greatest deviation from the analytical model being only 5.33% of the full scale predictions.

In the results from the PZT-8 [Figure 8(b)], the experimental data are slightly more scattered than those from the PZT-5H. Because of the decreased free displacement range of the PZT-8 (13 microns versus 50 microns for the PZT-5H), the imprecision of the measurements is more noticeable in this case, as the measurement of each deflection increment was closer to the limit of the precision of the equipment. The scatter in the data from the polymeric bimorph prototype is also more noticeable, because here a visual measurement was used to determine the position of the prototype. However, the gross slope of the experimental lines in all cases matches the analytical prediction well. Considering the simplicity of the model, the correspondence between the analytical model and the experimental data is good.

It is interesting to note that the line with maximum deviation is observed for the largest voltage on the PZT-5H prototype. The piezoelectric constant changes slightly with increasing applied voltage; piezoelectric materials are also subject to hysteresis. To keep the analytical model simple and easy to use, neither of these effects were included. These effects are much more pronounced in the PZT-5H piezoceramic than they are in the PZT-8. Another effect that was not included in the final simple model was the extension of the neutral axis. Although this effect is present in the unimorph ceramic actuators, as shown by the derivation, the magnitude of the effect is a factor of the nondimensional stiffness ratio, χ, and is thus small compared with the bending effect in these

Table 2. Error in case studies. Mean differences between analytical model and experimental data for three case studies: ceramic unimorph, polymeric bimorph, and four-layer polymeric multimorph.

Case Study and Material	Voltage (V)	Mean Difference in Force (milliNewtons)	Difference as % of Analytical Max. Force Value
Case 1: Ceramic unimorph	50	64.7	3.24%
PZT-5H [Figure 9(a)]	100	37.6	1.88%
	150	106.5	5.33%
Case 2: Ceramic unimorph	200	6.7	1.02%
PZT-8 [Figure 9(b)]	250	10.1	1.54%
	300	18.3	2.81%
	350	34.4	5.28%
	400	28.6	4.38%
Case 3: Polymeric bimorph	200	0.0712	3.40%
PVdF (Figure 12)	375	0.0598	1.76%
Case 4: Polymeric multimorph	200	0.193	0.59%
PVdF (Figure 13)	250	0.442	1.35%
	300	0.114	3.48%
	350	0.571	1.74%
	400	0.188	0.57%
Average Difference			2.56%

C-blocks. This effect is not present in the bimorph polymeric C-blocks because of their symmetric construction. Since all the errors are small and the errors present in the bimorph C-block are not noticeably smaller than those from the unimorph C-blocks, it can be concluded that the effect of neutral axis extension is small. Thus, despite the simplifying assumptions made during the development of the analytical model, the model predicts the observed experimental behavior of the individual C-blocks accurately enough for many engineering applications.

CONCLUSION

This paper presented the derivation of a force-deflection model for a generic individual C-block that accurately predicts the output force, output deflection, and stiffness of the C-block. This force-deflection model is a concise, linear law that depends on simple material and geometric parameters. The model was experimentally verified over a range of voltages using three case studies, ceramic unimorphs, polymeric bimorphs, and polymeric multimorphs. These three case studies offered a broad range of material parameters and geometric configurations over which to test the accuracy of the model. The average error for all voltage runs, when expressed as a percentage of the maximum force output, was 2.56% and the maximum error was only 5.33%. The results of the experimentation demonstrated that, although the model has a simple form, it is accurate.

The force-deflection model derived in this paper can be used to compare the performance of the C-block to that of an equivalent, commonly-used, straight bender. This comparison demonstrates that the C-block is 6.58 times as stiff, and produces 2.67 times the force, as the equivalent straight bender. The increase in force comes at the expense of deflection, as the C-block produces only 0.405 times the deflection as its straight counterpart. However, the total work that is available from the C-block is 8% more than the straight bender can produce; so overall the C-block compares favorably with the straight bender. The comparative performance of the C-block shows that the C-block architecture fits well within the mid-range stiffness gap between compliant straight benders and stiff stacks. Additionally, the increase in available energy from the C-block shows that the C-block is a more efficient architecture than the straight bender, and thus more efficient than other bending-mode actuators (Kugel, Chandran, and Cross, 1997).

The force-deflection model derived and tested for this paper completely describes the force and deflection behavior of a generic individual C-block actuator. Thus, this model will predict both the free deflection and the blocking force for any individual C-block actuator. This model also determines the overall stiffness of the C-block. Actuator stiffness is an important parameter, and is necessary to properly match the stiffnesses of the actuator and the application system, which will maximize the energy available from the actuator for useful work. The force-deflection model can also be used to determine the energy transfer from the actuator to the system. Thus, the entire quasi-static performance of a generic individual C-block can be accurately determined by using the force-deflection model derived in this paper.

Additionally, the model presented in this paper forms the basis for modeling more complex distributed arrays of C-block actuators. Distributed arrays add a dimension of ver-

satility to the individual C-block to allow simultaneous achievement of target force, deflection, stiffness, and energy transfer requirements. With the quasi-static performance of the individual C-block concisely modeled, the more versatile array architectures can be investigated.

ACKNOWLEDGEMENTS

The authors would like to thank the Army Research Office and the National Science Foundation for supporting this research under grant numbers DAAH04-96-1-0186 and CMS-952637, respectively.

REFERENCES

August, J. A. and S. P. Joshi. 1996. "Preliminary Design of Smart Structure Fins for High-Speed Missiles", in *Smart Structures and Materials 1996: Industrial and Commercial Applications of Smart Structures Technologies,* C. R. Crowe, ed., *Proc. SPIE,* 2721:58–65.

Bamford, R., C. P. Kuo, R. Glaser and B. K. Wada. 1995. "Long Stroke Precision PZT Actuator", in *AIAA/ASME/ASCE/AHS/ASC Structures, Structural Dynamics, and Materials Conference—Collection of Technical Papers,* New York: AIAA, 3278–3284.

Baz, A. and S. Poh. 1988. "Performance of an Active Control System with Piezoelectric Actuators," *Journal of Sound and Vibration,* 126:327–343.

Brei, D. 1994. "Design and Development of a Piezoelectric Microactuator Building Block for Deflection Improvement", in *Dynamic Systems and Control,* Vol. 2, DSC 55-2, New York: ASME, pp. 717–723.

Brei, D. 1995a. "Design and Development of a New Class of Piezoelectric Actuators for Force Improvement", in *Active Materials and Smart Structures,* G. L. Anderson and D. C. Lagoudas, eds., *Proc. SPIE,* 2427: 343–356.

Brei, D. 1995b. "Force-Deflection Behavior for C-Block Piezoelectric Actuator Architectures", in *Smart Structures and Materials 1995: Smart Structures and Integrated Systems,* I. Chopra, ed., *Proc. SPIE,* 2443:362–373.

Brei, D. J. Ervin and A. Moskalik. 1996. "Deflection-Voltage Performance of Asymmetrically Activated Piezoelectric C-Block Actuators", in *Smart Structures and Materials 1996: Smart Structures and Integrated Systems,* I. Chopra, ed., *Proc. SPIE,* 2717:276–286.

Damjanovic, D. and R. E. Newnham. 1992. "Electrostrictive and Piezoelectric Materials for Actuator Applications", *Journal of Intelligent Material Systems and Structures,* 3:190–208.

Dogan, A., K. Uchino and R. E. Newnham. 1997. "Composite Piezoelectric Transducer with Truncated Conical Endcaps Cymbal' ", *IEEE Transactions on Ultrasonics, Ferroelectrics, and Frequency Control,* 44(3): 597–605.

Fuller, C. R. and G. P. Gibbs. 1994. "Active Control of Interior Noise in a Business Jet Using Piezoelectric Actuators", *Proceedings, 1994 National Conference on Noise Control Engineering,* Poughkeepsie, NY: Institute of Noise Control Engineering, pp. 389–394.

Giurgiutiu, V., Z. Chaudhry and C. A. Rogers. 1995. "Stiffness Issues in the Design of ISA Displacement Amplification Devices: Case Study of Hydraulic Displacement Amplifier", in *Smart Structures and Materials 1995: Smart Structures and Integrated Systems,* I. Chopra, ed., *Proc. SPIE,* 2443:105–119.

Haertling, G. H. 1994. "Ultra-High-Displacement Actuator", *American Ceramic Society Bulletin,* 73(2):93–96.

Hall, S. R. and E. F. Prechtl. 1996. "Development of a Piezoelectric Servoflap for Helicopter Rotor Control", *Smart Materials and Structures,* 5:26–34.

Kudva, J., P. Jardine, C. Martin and K. Appa. 1996. "Overview of the ARPA/WL 'Smart Structures and Materials Development—Smart Wing' Contract", in *Smart Structures and Materials 1996: Industrial and Commercial Applications of Smart Structures Technologies,* C. R. Crowe, ed., *Proc. SPIE,* 2721:10–16.

Kugel, V. D., S. Chandran and L. E. Cross. 1997. "Comparative Analysis of Piezoelectric Bending-Mode Actuators", in *Smart Structures and Materials 1997: Smart Materials Technologies,* W. C. Simmons, I. A. Aksay and D. R. Huston, eds., *Proc. SPIE,* 3040:70–80.

Larson, P. H. and J. R. Vinson, 1993. "The Use of Piezoelectric Materials in Curved Beams and Rings", *Adaptive Structures and Material Systems,* AD-Vol. 35, New York: ASME, pp. 277–285.

Martinez, D. R., T. D. Hinnerichs and J. M. Redmond. 1996. "Vibration Control for Precision Manufacturing Using Piezoelectric Actuators", *Journal of Intelligent Material Systems and Structures,* 7:182–191.

Moskalik, A. J. and D. E. Brei. 1995. "Deflection-Voltage Behavior of Individual Polymeric Multilayer Arched Piezoelectric Actuators", AMSE Paper 95-WA/AD-8, New York: ASME.

Onitsuka, K., A. Dogan, J. F. Tressler, Q. Xu, S. Yoshikawa and R. E. Newnham. 1995. "Metal-Ceramic Composite Transducer, the'Moonie' ", *Journal of Intelligent Material Systems and Structures,* 6:447–455.

Paine, J. S. N. and Z. Chaudhry. 1996. "The Impact of Amplification on Efficiency and Energy Density of Induced Strain Actuators", in *Proceedings of the ASME Aerospace Division,* AD-Vol. 52, J. C. I. Chang, J. Coulter, D. Brei, D. Martinez, W. Ng and P. P. Feidman, eds., New York: ASME, pp. 511–516.

Qatu, M. S. 1993. "Theories and Analyses of Thin and Moderately Thick Laminated Composite Curved Beams", *International Journal of Solids and Structures,* 30(20):2743–2756.

Samak, D. K. and I. Chopra. 1993. "A Feasibility Study to Build a Smart Rotor: Trailing Edge Flap Actuation", *Smart Structures and Materials 1992: Smart Structures and Intelligent Systems,* N. W. Hagood and G. J. Knowles, eds., *Proc. SPIE,* 1917:225–237.

Samak, D. K. and I. Chopra. 1996. "Design of High Force, High Displacement Actuators for Helicopter Rotors", *Smart Materials and Structures,* 5:58–67.

Staveley. (no date). "EBL Piezoceramic Tubes for Ultraprecise Positioning Applications" (brochure), available from Staveley Sensors, 91 Prestige Park Circle, East Hartford, CT 06108-1918.

Sumali, H. and H. Cudney. 1994. "An Active Engine Mount with a Piezoelectric Stacked Actuator", *Proceedings of the 35th SDM Conference,* New York: AIAA, pp. 1233–1241.

Thirupathi, S. R. and N. G. Naganathan. 1992. "Use of Piezoceramic Actuation for Automotive Active Suspension Mechanisms: A Feasibility Study", *Robotics, Spatial Mechanisms, and Mechanical Systems,* New York: ASME, pp. 233–241.

Yang, R., M. Jouaneh and R. Schweizer. 1996. "Design and Characterization of a Low-Profile Micropositioning Stage", *Precision Engineering,* 18:20–29.